

Improved single particle localization accuracy with dual objective multifocal plane microscopy

Sripad Ram[†], Prashant Prabhat^{†*}, E. Sally Ward[†] and Raimund J. Ober^{†*}

[†]*Department of Immunology, University of Texas Southwestern Medical Center, Dallas, TX 75390.*

^{*}*Department of Electrical Engineering, University of Texas at Dallas, Richardson, TX 75083.*

ober@utdallas.edu

www4.utsouthwestern.edu/wardlab

Abstract: In single particle imaging applications, the number of photons detected from the fluorescent label plays a crucial role in the quantitative analysis of the acquired data. For example, in tracking experiments the localization accuracy of the labeled entity can be improved by collecting more photons from the labeled entity. Here, we report the development of dual objective multifocal plane microscopy (dMUM) for single particle studies. The new microscope configuration uses two opposing objective lenses, where one of the objectives is in an inverted position and the other objective is in an upright position. We show that dMUM has a higher photon collection efficiency when compared to standard microscopes. We demonstrate that fluorescent labels can be localized with better accuracy in 2D and 3D when imaged through dMUM than when imaged through a standard microscope. Analytical tools are introduced to estimate the nanoprobe location from dMUM images and to characterize the accuracy with which they can be determined.

© 2009 Optical Society of America

OCIS codes: (180.2520) Fluorescence Microscopy.

References and links

1. M. J. Saxton and K. Jacobson, "Single particle tracking : applications to membrane dynamics," *Annu. Rev. Biophys. Biomol. Struct.* **26**, 373–399 (1997).
2. X. Michalet, A. N. Kapanidis, T. Laurence, F. Pinaud, S. Doose, M. Pflughoeft, and S. Weiss, "The power and prospects of fluorescence microscopies and spectroscopies," *Annu. Rev. Biophys. Biomol. Struct.* **32**, 161–182 (2003).
3. E. Toprak, H. Balci, B. H. Blehm, and P. R. Selvin, "Three-dimensional particle tracking via bifocal imaging," *Nano Lett.* **7**, 2043–2045 (2007).
4. G. J. Schütz, J. Hesse, G. Freudenthaler, V. P. Pastushenko, H. G. Knaus, B. Pragl, and H. Schindler, "3D mapping of individual ion channels on living cells," *Single Molecules* **2**, 153–157 (2000).
5. R. J. Ober, S. Ram, and E. S. Ward, "Localization accuracy in single molecule microscopy," *Biophys. J.* **86**, 1185–1200 (2004).
6. M. P. Gordon, T. Ha, and P. R. Selvin, "Single molecule high resolution imaging with photobleaching," *Proc. Natl. Acad. Sci. USA* **101**, 6462–6465 (2004).
7. S. Ram, E. S. Ward, and R. J. Ober, "Beyond Rayleigh's criterion: a resolution measure with application to single-molecule microscopy," *Proc. Natl. Acad. Sci. USA* **103**, 4457–4462 (2006).

8. K. A. Lidke, B. Rieger, T. M. Jovin, and R. Heintzmann, "Superresolution by localization of quantum dots using blinking statistics," *Opt. Express* **13**, 7052–7062 (2005).
9. S. Ram, P. Prabhat, J. Chao, E. S. Ward, and R. J. Ober, "High accuracy 3D quantum dot tracking with multifocal plane microscopy for the study of fast intracellular dynamics in live cells," *Biophys. J.* **95**, 6025–6043 (2008).
10. L. Holtzer, T. Meckel, and T. Schmidt, "Nanometric three-dimensional tracking of individual quantum dots in cells," *Appl. Phys. Lett.* **90**, 053902 (2007).
11. E. Betzig, G. H. Patterson, R. Sougrat, O. W. Lindwasser, S. Olenych, J. S. Bonifacino, M. W. Davidson, J. Lippincott-Schwartz, and H. F. Hess, "Imaging intracellular fluorescent proteins at nanometer resolution," *Science* **313**, 1642–1645 (2006).
12. A. Sharonov and R. M. Hochstrasser, "Wide-field subdiffraction imaging by accumulated binding of diffusing probes," *Proc. Natl. Acad. Sci. USA* **103**, 18911–18916 (2006).
13. J. G. Ritter, R. Veith, J. P. Siebrasse, and U. Kubitscheck, "High-contrast single-particle tracking by selective focal plane illumination microscopy," *Opt. Express* **16**, 7142–7152 (2008).
14. A. Agrawal, R. Deo, G. D. Wang, M. D. Wang, and S. Nie, "Nanometer-scale mapping and single-molecule detection with color-coded nanoparticle probes," *Proc. Natl. Acad. Sci. USA* **105**, 3298–3303 (2008).
15. V. Levi, Q. Ruan, and E. Gratton, "3-D particle tracking in a two-photon microscope: application to the study of molecular dynamics in cells," *Biophys. J.* **88**, 2919–2928 (2005).
16. M. Speidel, A. Jonáš, and E. L. Florin, "Three-dimensional tracking of fluorescent nanoparticles with sub-nanometer precision by use of off-focus imaging," *Opt. Lett.* **28**, 69–71 (2003).
17. H. Cang, C. S. Xu, D. Montiel, and H. Yang, "Guiding a confocal microscope by single fluorescent nanoparticles," *Opt. Lett.* **32**, 2729–2731 (2007).
18. A. J. Berglund and H. Mabuchi, "Tracking-FCS: fluorescence correlation spectroscopy of individual particles," *Opt. Express* **13**, 8069–8082 (2005).
19. G. A. Lessard, P. M. Goowin, and J. H. Werner, "Three-dimensional tracking of individual quantum dots," *Appl. Phys. Lett.* **91**, 224106 (2007).
20. S. Djidel, J. K. Gansel, H. I. Campbell, and A. H. Greenaway, "High speed, 3-dimensional telecentric imaging," *Opt. Express* **14**, 8269–8277 (2006).
21. W. Amir, R. Carriles, E. Hoover, T. A. Planchon, C. G. Durfee, and J. A. Squier, "Simultaneous imaging of multiple focal planes using a two-photon scanning microscope," *Opt. Lett.* **32**, 1731–1733 (2007).
22. J. Rosen and G. Brooker, "Non-scanning motionless fluorescence three-dimensional holographic microscopy," *Nature Photonics* **2**, 190–195 (2008).
23. S. Ram, E. S. Ward, and R. J. Ober, "A stochastic analysis of performance limits for optical microscopes," *Multidimensional Systems and Signal Processing* **17**, 27–58 (2006).
24. N. Bobroff, "Position measurement with a resolution and noise limited instrument," *Rev. Sci. Instrum.* **57**, 1152–1157 (1986).
25. U. Kubitscheck, O. Kückmann, T. Kues, and R. Peters, "Imaging and tracking single GFP molecules in solution," *Biophys. J.* **78**, 2170–2179 (2000).
26. R. E. Thompson, D. R. Larson, and W. W. Webb, "Precise nanometer localization analysis for individual fluorescent probes," *Biophys. J.* **82**, 2775–2783 (2002).
27. S. Ram, E. S. Ward, and R. J. Ober, "How accurately can a single molecule be localized in three dimensions using a fluorescence microscope?" *Proceedings of the SPIE* **5699**, 426–435 (2005).
28. F. Aguet, D. V. D. Ville, and M. Unser, "A maximum likelihood formalism for sub-resolution axial localization of fluorescent nanoparticles," *Opt. Express* **13**, 10503–10522 (2005).
29. J. Chao, S. Ram, A. V. Abraham, E. S. Ward, and R. J. Ober, "A resolution measure for three-dimensional microscopy," *Opt. Commun.* **282**, 1751–1761 (2009).
30. T. Ruckstuhl, J. Enderlein, S. Jung, and S. Seeger, "Forbidden light detection from single molecules," *Anal. Chem.* **72**, 2117–2123 (2000).
31. A. P. Alivisatos, W. Gu, and C. Larabell, "Quantum dots as cellular probes," *Annu. Rev. Biomed. Engg.* **7**, 55–76 (2005).
32. S. W. Hell and E. H. Stelzer, "Properties of a 4Pi confocal fluorescence microscope," *J. Opt. Soc. Am. A* **9**, 2156–2166 (1992).
33. S. W. Hell and E. H. Stelzer, "Fundamental improvement of resolution with a 4Pi-confocal fluorescence microscope using two-photon excitation," *Opt. Commun.* **93**, 277–282 (1992).
34. M. G. Gustafsson, D. A. Agard, and J. W. Sedat, "Sevenfold improvement of axial resolution in 3D widefield microscopy using two objective lenses," *Proceedings of the SPIE* **2412**, 147–156 (1995).
35. M. G. Gustafsson, "Extended resolution fluorescence microscopy," *Curr. Opin. Struct. Biol.* **9**, 627–634 (1999).
36. E. Betzig, "Excitation strategies for optical lattice microscopy," *Opt. Express* **13**, 3021–3036 (2005).
37. P. Prabhat, S. Ram, E. S. Ward, and R. J. Ober, "Simultaneous imaging of different focal planes in fluorescence microscopy for the study of cellular dynamics in three dimensions," *IEEE Transactions on Nanobioscience* **3**, 237–242 (2004).
38. S. Ram, J. Chao, P. Prabhat, E. S. Ward, and R. J. Ober, "A novel approach to determining the three-dimensional location of microscopic objects with applications to 3D particle tracking," *Proceedings of the SPIE* **6443**, D1–D7

- (2007).
39. P. Prabhat, Z. Gan, J. Chao, S. Ram, C. Vaccaro, S. Gibbons, R. J. Ober, and E. S. Ward, "Elucidation of intracellular pathways leading to exocytosis of the Fc receptor, FcRn, using multifocal plane microscopy," *Proc. Natl. Acad. Sci. USA* **104**, 5889–5894 (2007).
 40. www4.utsouthwestern.edu/wardlab/miatool.
 41. <http://www4.utsouthwestern.edu/wardlab/estimationTool>.
 42. <http://www4.utsouthwestern.edu/wardlab/FandPLimitTool>.
 43. MATLAB, *Image processing toolbox user guide ver 3.0* (The MathWorks Inc, USA, 2001).
 44. M. Born and E. Wolf, *Principles of Optics* (Cambridge University Press, Cambridge, UK, 1999).
 45. C. R. Rao, *Linear statistical inference and its applications*. (Wiley, New York, USA., 1965).
 46. M. Bates, B. Huang, G. T. Dempsey, and X. Zhuang, "Multicolor super-resolution imaging with photo-switchable fluorescent probes." *Science* **317**, 1749–1753 (2007).
 47. S. F. Gibson and F. Lanni, "Diffraction by a circular aperture as a model for three-dimensional optical microscopy," *J. Opt. Soc. Am. A* **6**, 1357–1367 (1989).
 48. P. Török, P. Varga, and G. R. Booker, "Electromagnetic diffraction of light focussed through a planar interface between materials of mismatched refractive indices: structure of the electromagnetic field. I," *J. Opt. Soc. Am. A* **12**, 2136–2144 (1995).
-

1. Introduction

Single particle tracking is a powerful tool to study biological processes at the cellular and molecular level ([1, 2]). Single particle studies remove ensemble averaging effects that are characteristic of bulk studies and can provide information on the behavior of individual molecules. Such information becomes particularly important when the system under study is highly heterogeneous as is the case in a cellular environment. In the recent past several new techniques have been reported to image single fluorescent point sources in two and three dimensions at nanoscale precision and resolution ([3, 4, 5, 6, 7, 8, 9, 10, 11, 12, 13, 14, 15, 16, 17, 18, 19]). Moreover, there has also been significant interest in developing imaging modalities for rapid 3D imaging and tracking of sub-cellular objects in cells ([20, 21, 22]).

In single particle imaging applications the number of detected photons from the labeled entity plays a crucial role in the analysis of the acquired data. For instance, it has been shown that the limit to the 2D localization accuracy of the nanoprobe (i.e., best possible accuracy with which the 2D location can be determined) can be improved by collecting more photons from the nanoprobe ([5, 23, 24, 25, 26]). In the noise free case, the limit of the localization accuracy typically scales as $1/\sqrt{N}$, where N denotes the number of detected photons from the nanoprobe. A similar behavior of the limit of the localization accuracy has also been reported for the 3D localization problem ([27, 28, 9]). In the resolution problem, the accuracy with which the distance between two point sources can be determined is improved by collecting more photons from the point sources ([7, 29]). Hence achieving a high photon collection efficiency is important in such studies.

Microscope setups that are used for single particle experiments are typically constructed from components that have high light collection, detection, or transmission efficiency. Examples include the use of high numerical aperture objective lenses and the use of highly sensitive imaging detectors. Past efforts to improve the light collection efficiency of optical microscopes have been directed towards increasing the numerical aperture of the objective lens. For example, the use of a high numerical aperture parabolic mirror objective was demonstrated in a confocal imaging configuration ([30]) to have superior light collection efficiency than a standard objective. Aside from technological advances, there has also been significant effort in developing bright and photostable fluorescent labels to obtain higher photon counts. For example, the introduction of quantum dots ([31]) and other fluorescent nanoparticles have provided beneficial alternatives to conventional fluorophores.

Currently, particle tracking experiments are typically carried out on either an inverted or an upright microscope, in which a single objective lens illuminates the sample and also collects the

fluorescence signal from it. Note that although fluorescence emission from the sample occurs in all directions (i.e., above and below the sample), the use of a single objective lens in these microscope configurations results in collecting light from only one side of the sample. Even if a high numerical aperture objective lens is used, not all photons emitted at one side of the sample can be collected due to the finite collection angle of the objective lens. Thus even under the best imaging conditions conventional microscopes collect only a fraction of the photons emitted from the sample.

Here we report the use of a microscope configuration that uses two opposing objective lenses for imaging the sample. We refer to this configuration as dual objective multifocal plane microscopy (dMUM). In dMUM, one of the objective lens is in an inverted position, while the other objective lens is in an upright position (see Fig. 1). The sample is illuminated in widefield mode through one of the objective lenses, analogous to the way the sample is illuminated in a standard microscope. The emitted fluorescence is collected by both objective lenses. Hence for a given illumination condition, dMUM detects the fluorescence from above and below the sample, and as a result collects more photons than a standard microscope.

The use of opposing objective lenses is not new and has been reported previously, for example, in the implementation of 4pi confocal microscopy ([32, 33]) and I5M ([34]). These techniques use interference based illumination schemes to produce a narrow 3D intensity distribution of the detected photons. This results in significantly improved axial resolution when compared to regular widefield or confocal microscopes. The narrow intensity distribution profile may also lead to improved localization accuracy of point sources. An analysis by Gustafsson ([35]) suggests that these techniques may, however, have reduced photon count capabilities due to several factors such as the use of confocal pinhole, low numerical aperture objectives, etc. Another application of opposing objective lenses is a recent proposal for generating a three-dimensional lattice of focal spots with the potential for 3D cellular imaging applications ([36]). The dMUM configuration reported here is demonstrated for imaging single fluorescent point emitters with improved photon collection efficiency.

We perform imaging experiments with a mono-plane, nanoprobe sample and consider two specific imaging configurations of dMUM, namely 2D infocus imaging and 3D imaging configurations. In the 2D infocus imaging configuration, the objective lenses are focused on the sample. This configuration can be used in place of the classical 2D conventional microscope to image processes that are typically confined to two dimensions, for example, membrane receptor dynamics on the cell surface. The 3D imaging configuration exploits the multifocal plane imaging capability of dMUM in which the sample is imaged at two different focus levels by focusing the objective lenses at distinct planes. This configuration can be used for 3D tracking experiments and importantly high accuracy z-localization, for example, to study protein transport inside a cell. We demonstrate experimentally that in the 2D infocus imaging configuration the x- and y-location coordinates of the nanoprobe can be determined with significantly better accuracy from dMUM when compared to a standard microscope. We also show using experimental data that in the 3D imaging configuration, dMUM provides high z-localization accuracy. Using analytical calculations based on the Fisher information matrix, we compare the z-localization capability of dMUM, conventional microscopy and multifocal plane microscopy (MUM), an imaging modality that we previously developed, which also supports multifocal plane imaging ([37, 39]). We show that the 3D imaging configuration of dMUM provides consistently better z-localization accuracy than a standard microscope and MUM. We have also validated the improved z-localization accuracy of dMUM over MUM through simulations.

2. Materials and methods

2.1. Dual objective multifocal plane microscopy

The dual objective imaging configuration was built using two inverted Zeiss microscopes (AxioObserver), where one of the microscopes ('top scope') was mounted in an 'upside down' orientation on linear X-Y translation stages which were attached to the other microscope ('bottom scope'). The sample was placed in the bottom scope and the objective in the top scope was attached to the nose piece through C-mount spacers in order for it to reach the sample.

2.2. Sample preparation

A bead sample was prepared by diluting 100 nm Tetraspeck beads (Invitrogen, Carlsbad, CA) 500 fold in water and incubating 200 μ l of the diluted sample on a poly-lysine coated MatTek dish (MatTek Corporation, Ashland, MA). After 2 hours unbound and freely floating beads were removed (by aspirating the water) resulting in a mono-plane distribution of beads and 1 mL of fresh water was added and the sample was imaged.

A quantum dot (QD) sample (QDot® 655, Invitrogen, Carlsbad, CA) was prepared by diluting QDs to a final concentration of 100 pM in a Tris buffer (10 mM TrisHCl, 50 mM NaCl) containing 27.5 mM 2-mercaptoethanol and 200 μ l of the diluted QD sample was incubated on a poly-lysine coated MatTek dish. After 1 hour, unbound QDs were removed (resulting in a mono-plane distribution of the QDs) and 200 μ l of Tris buffer containing 27.5 mM 2-mercaptoethanol was added and the sample was immediately imaged.

2.3. Imaging experiments

The specific configuration of dMUM implemented here consists of a Zeiss Acroplan 63x, NA 0.95 water dipping objective in the top scope and a Zeiss C-Apochromat 63x, NA 1.2 water immersion objective in the bottom scope. The sample was epi-illuminated with a 543 nm laser line (Research Electro-Optics Inc., Boulder, CO) through the bottom scope. The light from the sample passed through a 488/543/633M emission filter in the bottom scope and in the top scope (all filters are from Chroma Technology, Battlebro, VT). A Hamamatsu CCD camera (C8484, Hamamatsu Corp., Bridgewater, NJ) was used to capture the fluorescence signal in the bottom scope and an Andor iXon camera (DV887, Andor Technologies, South Windsor, CT) was used to capture the fluorescence signal in the top scope. The Andor camera was operated in conventional gain mode. The exposure times of the cameras were set to 0.3 s.

2.4. X-Y location estimation from dMUM images - 2D infocus imaging configuration

All data processing, analysis and visualization were carried out in custom written software packages MIATool ([40]), EstimationTool ([41]) and FandPLimitTool ([42]) in the MATLAB programming language (The MathWorks Inc., Natick, MA). The 2D location of the fluorescent nanoprobe was determined by simultaneously fitting an Airy profile to the images captured in the two CCD cameras. From each acquired image, a small region of interest (ROI) containing the nanoprobe image was selected. Prior to curve fitting, the pixel values in the ROI were converted to photon counts by subtracting the constant offset from each pixel value and then multiplying it by the conversion factor. The constant offset and the conversion factor were taken from the specification sheet provided by the camera manufacturer.

The intensity distributions of the ROIs from the top and bottom scope cameras are modeled by image profiles μ_{θ}^t and μ_{θ}^b , respectively, which are given by

$$\mu_{\theta}^b(l, t) = \frac{A_b t_b}{\pi M_b^2} \iint_{C_l} \frac{J_1^2(a_b \sqrt{(x - M_b x_0)^2 + (y - M_b y_0)^2})}{(x - M_b x_0)^2 + (y - M_b y_0)^2} dx dy + B_{b,l} t_b, \quad (1)$$

$$\mu_{\theta}^l(k, t) = \frac{A_t t_l}{\pi M_t^2} \iint_{C_k} \frac{J_1^2(a_t \sqrt{(x - M_t f_x(x_0, y_0))^2 + (y - M_t f_y(x_0, y_0))^2})}{(x - M_t f_x(x_0, y_0))^2 + (y - M_t f_y(x_0, y_0))^2} dx dy + B_{t,k} t_l, \quad (2)$$

where C_k (C_l) denotes the region on the detector plane occupied by the k^{th} (l^{th}) pixel, $k = 1, \dots, N_t$ ($l = 1, \dots, N_b$) and N_t (N_b) denotes the total number of pixels in the ROI selected from the top (bottom) scope image.

Equations 1 and 2 describe the images of a nanoprobe in the 2D imaging scenario in which the sample is in focus with respect to both objective lenses. In the above Eqs., (x_0, y_0) denotes the location of the nanoprobe in the sample, $\{f_x, f_y\}$ denotes the mapping function that maps the X-Y coordinates of an arbitrary point in the bottom scope image to the top scope image (see Section 2.4.1), J_1 denotes the first order Bessel function of the first kind, M_t and M_b ($n_{a,t}$ and $n_{a,b}$) denote the magnification (numerical aperture) of the objectives used in the top and bottom scopes, respectively, $a_t = 2\pi n_{a,t}/M_t$, $a_b = 2\pi n_{a,b}/M_b$, A_t and A_b denote the photon detection rate of the nanoprobe in the top and bottom scopes, respectively, t_t and t_b denote the exposure times of the cameras in the top and bottom scopes, respectively, $\{B_{t,1}, \dots, B_{t,N_t}\}$ and $\{B_{b,1}, \dots, B_{b,N_b}\}$ denote the photon detection rate of the background component at each pixel in the ROIs of images acquired from the top and bottom scopes, respectively, and $\theta = (x_0, y_0, a_b, a_t)$.

The following protocol was used to estimate the 2D location. For each ROI the photon detection rate of the background component, which was assumed to be a constant over the ROI, was estimated by taking the mean of the photon count from the four corner pixels of that ROI and dividing it by the exposure time. Then the photon detection rate for the top and bottom scope images were independently estimated by subtracting the background photons (product of the background photon detection rate and exposure time) from each pixel, summing the resulting values over all the pixels in the ROI and then dividing the sum by the exposure time. The X-Y coordinates of the nanoprobe along with a_t and a_b were determined by simultaneously fitting eqs. 1 and 2 to the bottom and top scope ROIs, respectively, using a global maximum likelihood estimation algorithm, which was implemented through the MATLAB optimization toolbox. During curve fitting, the background and photon detection rate were fixed to their corresponding pre-calculated values.

2.4.1. Determination of the mapping function

The following procedure was used to determine the mapping function $\{f_x, f_y\}$ that maps the X-Y coordinates of a point in the bottom scope image to the top scope image. For every acquired image, a local mapping function was determined for each nanoprobe whose X-Y coordinates were estimated from the dMUM images. For a given nanoprobe, several neighboring nanoprobe (about 5-6) were chosen as fiducial markers. The X-Y coordinates of the fiducial markers in the top and bottom scopes were independently determined by fitting Airy profiles to their top and bottom scope images. Using the X-Y coordinates of the fiducial markers, a mapping function was obtained that maps the X-Y coordinates of an arbitrary point in the bottom scope image to the top scope image in the vicinity of the nanoprobe whose X-Y coordinates are to be determined from dMUM images. We assumed the mapping function to be a projective transformation ([43]), which corrects for translation, rotation, scaling and shearing.

2.4.2. Drift correction

Due to the presence of stage drift, the X-Y location estimates obtained from the experimental data exhibit a systematic drift in their numerical values. In order to compare the experimental accuracy (standard deviation) of the estimates with the theoretical accuracy (2D localization measure), drift correction had to be carried out on the estimates before calculating their standard

deviations. This was done by using the location coordinates of the nanoprobe that were used as fiducial markers for determining the mapping function (see above). For each acquired image, a map was generated that maps the X-Y coordinates of the fiducial markers in that frame to the X-Y coordinates of the fiducial markers in the first frame. The map was assumed to be a projective transformation ([43]). Separate maps were generated for the top and bottom scope images and were used to correct for the drift in the independent X-Y estimates reported in Table 1. The X-Y estimates obtained using the dMUM images were drift corrected with the map generated for the bottom scope image, since the 2D location estimation algorithm used on the dMUM images estimates the bottom scope X-Y coordinates (see Section 2.4).

2.5. Estimating the z-location from dMUM images - 3D imaging configuration

Previously we developed an algorithm, the MUM localization algorithm (MUMLA), to determine the z-position of a fluorescent point source from images that were simultaneously acquired at multiple focal planes ([9]). Here we use MUMLA to estimate the z-location of the nanoprobe from simulated and experimental data. For simulations, we consider a dMUM (MUM) setup with the distance between the two focal planes set to 1 μm . The dMUM and MUM images of the nanoprobe at different defocus levels were simulated using the Born and Wolf model of the 3D point spread function ([44]) as described in [9]. The pixel values in the simulated images are in photon counts, since MUMLA works on the photon count data.

The z-position of the nanoprobe from simulated and experimental data was determined as described in [9]. Briefly, the z-position of the nanoprobe was estimated by simultaneously fitting a pair of 3D point spread function profiles (Born and Wolf model) to the dMUM (MUM) image using a global maximum likelihood algorithm that was implemented through the MATLAB optimization toolbox.

2.6. Localization measure calculations

By definition, the localization measure provides a limit to the accuracy with which the location of a nanoprobe can be estimated for a specific imaging condition. Our approach to calculate the localization measure is based on the statistical theory concerning the Fisher information matrix ([45]). A detailed discussion of this approach has been published elsewhere ([5, 23]) and here we provide a brief description. According to the Cramer-Rao inequality ([45]), the covariance of any unbiased estimator $\hat{\theta}$ of an unknown parameter θ is always bounded from below by the inverse Fisher information matrix, i.e., $\text{Cov}(\hat{\theta}) \geq \mathbf{I}^{-1}(\theta)$. By definition, the Fisher information matrix $\mathbf{I}(\theta)$ provides a quantitative measure of the total information contained in the acquired image about the parameter θ and is independent of how θ is estimated. Because the performance of estimators is typically specified in terms of its standard deviation, the Cramer-Rao inequality implies that the square root of the Fisher information matrix provides a lower bound to the accuracy with which θ can be determined. For the location estimation problem, the square root of the leading diagonal entries of $\mathbf{I}(\theta)$ provides a limit to the localization accuracy of the fluorescent nanoprobe, and we refer to this as the localization measure.

To calculate the localization measure for the various microscope configurations, we require analytical expressions of the Fisher information matrix for the problem of estimating the 2D/3D location of a nanoprobe for that particular microscope configuration. The analytical expression of the Fisher information matrix for the 2D/3D location estimation problem for dMUM is given by

$$\mathbf{I}(\theta) = \mathbf{I}_t(\theta) + \mathbf{I}_b(\theta), \quad \theta \in \Theta, \quad (3)$$

where Θ denotes the parameter space, $\mathbf{I}_t(\theta)$ ($\mathbf{I}_b(\theta)$) denotes the Fisher information matrix for the image acquired in the top (bottom) scope. The analytical expressions for $\mathbf{I}_t(\theta)$ and $\mathbf{I}_b(\theta)$ are analogous to those of a standard microscope, which has been published before for the 2D

and 3D location estimation problems (see [5, 23, 27]). The analytical expression for the 3D location estimation problem for a two plane MUM setup is analogous to Eq. 3 and has been published elsewhere ([9]).

In Fig. 3 we have plotted the 2D and 3D localization measures for the various microscope configurations. For all the plots, we consider a practical imaging scenario in which the acquired data is pixelated and contains additive noise sources. In particular we consider additive Poisson noise, which, for example, models the background component in the acquired data and additive Gaussian noise, which, for example, models the readout noise of the imaging detector. In addition to pixelation and additive noise sources, the 2D/3D localization measure calculations also take into account the stochastic nature of the detected photons from the point source at each pixel, which is modeled as an independent Poisson random variable (see [23] for details).

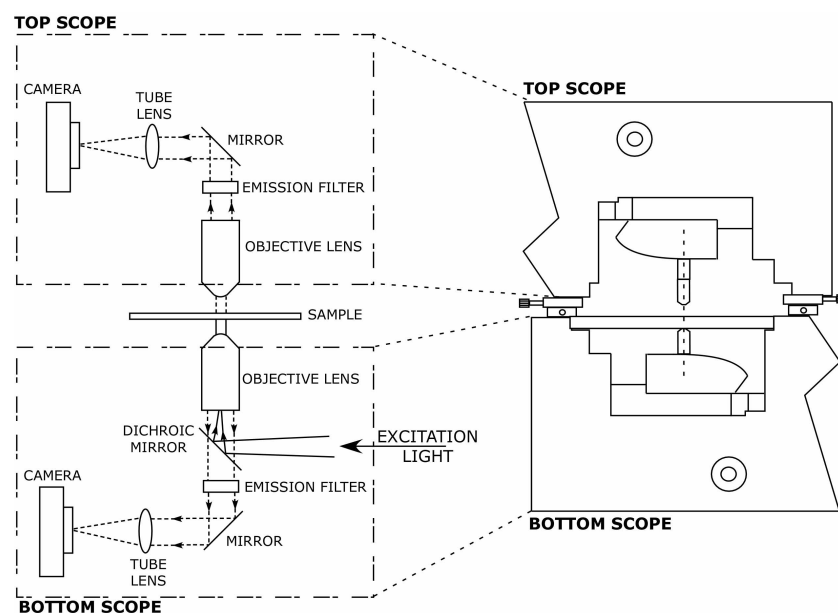


Fig. 1. Dual objective multifocal plane microscope. The figure shows a schematic of dMUM that is capable of imaging the sample from top and bottom. Our specific implementation of the dMUM imaging configuration used two inverted microscopes (Zeiss AxioObserver), where one of the microscopes (top scope) was in an upside down orientation and mounted on linear translation stages that were then attached to the other microscope (bottom scope).

3. Results

3.1. dMUM imaging configuration

The dMUM configuration proposed here enables the imaging of the sample from both the top and the bottom (see Fig. 1). This is achieved by using two inverted microscope bodies, where one of the bodies is oriented in an upside down position (top scope) and mounted on the other microscope body (bottom scope) through linear translation stages. The sample is illuminated in widefield mode through the bottom scope. The fluorescence light from the sample is collected by objective lenses in the top and bottom scope and passes through emission filters. In each microscope, the collected fluorescence signal is focused onto a CCD camera. Prior to acquiring images from the sample, the top scope is aligned with the help of the translation stages to ensure

that the objectives of the top and bottom scopes image the same field of view in the sample. Fig. 2 shows a dMUM image of a 100 nm tetraspeck bead sample (panel a) and a QD sample (panel b), which were acquired using the 2D infocus imaging configuration. The figure also shows a dMUM image of a 100 nm tetraspeck bead sample (panel c) which pertains to the 3D imaging configuration. The images shown are the raw data which are not spatially registered. Note that there is a scale change between the top and bottom scope images due to the fact that the cameras used to acquire the images in the top and bottom scopes have different pixel sizes.

3.2. *Photon collection efficiency of dMUM*

To verify the improved light collection capability of dMUM over a standard microscope, we calculated the number of detected photons from the nanoprobe in the acquired data (Fig. 2). Because of the use of different objectives and cameras in the top and bottom scopes, for a given nanoprobe the number of photons detected were different in the two scopes. For example, for the bead (QD) highlighted with an arrowhead in Fig. 2(a) (Fig. 2(b)), 8770 (8700) photons and 4750 (3100) photons were collected from the top and bottom cameras, respectively, when the exposure time of both cameras was 300 ms. Note that a higher photon count is observed in the top camera although a lower NA objective is used in the top scope. This is due to the fact that the quantum efficiency of the camera in the top scope is higher than the quantum efficiency of the camera in the bottom scope. Also, note that the ratio of photon counts between the top and bottom scopes for the bead and QD are different due to differences in the spectral sensitivities of the two cameras.

3.3. *Comparison of dMUM and standard microscope for X-Y location estimation - 2D infocus imaging configuration*

We next wanted to determine the 2D location of the nanoprobe from dMUM images acquired in the 2D infocus imaging configuration (Figs. 2(a) and 2(b)). In order to achieve improved localization, we require a methodology that make use of the additional photon counts available in the dMUM images. For this, we have developed an estimation algorithm that simultaneously fits an Airy profile to the nanoprobe images acquired in the top and bottom scopes (see Section 2.4). For comparison purposes, the 2D location of the nanoprobe was also independently determined from the image acquired from the top (bottom) scope only, which pertains to a standard optical microscope. This was done by fitting separate Airy profiles to the data acquired from the top and bottom scopes. The results of the 2D location estimation are given in Table 1, which lists the standard deviations of the X-Y location estimates of several nanoprobe from the infocus images acquired in dMUM, top scope and bottom scope. Due to stage drift, the X-Y estimates were drift corrected prior to calculating their standard deviation. From the table we see that the accuracy (i.e., standard deviation) of the 2D location estimates from the infocus images for dMUM is consistently better than the accuracy obtained from only the top or the bottom scope. In particular, we see that the X-Y accuracy for dMUM is about 20% - 35% better than the X-Y accuracy when independently estimated as in a conventional microscope.

Note that the X-Y accuracy for the bottom scope is consistently better than the X-Y accuracy for the top scope even though the bottom scope collects less photons than the top scope. This can be attributed in part to the fact that the objective lens in the top scope has a lower numerical aperture than the objective lens in the bottom scope. Previously, it has been shown by us that the accuracy of the X-Y coordinates not only depends on the number of detected photons, but also on other parameters such as the numerical aperture of the objective lens ([5]).

It should be pointed out that for the bottom scope (and for dMUM), the standard deviation of the x-coordinate estimates is consistently larger than the standard deviation of the y-coordinate estimates. This behavior is due to the residual effects of drift correction, which arise due to

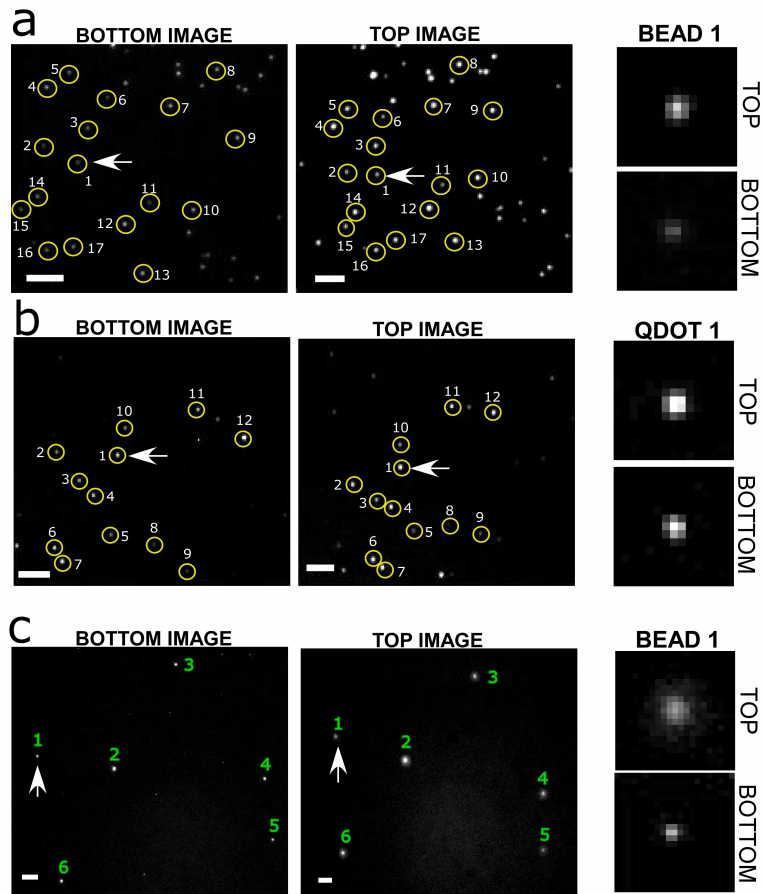


Fig. 2. dMUM images of nanoprobe samples. Panels a and b show dMUM images of a 100 nm tetraspeck bead sample and a QD655 sample, respectively, and pertain to the 2D infocus imaging configuration. Panel c shows a dMUM image of a 100 nm tetraspeck bead sample that pertains to the 3D imaging configuration. This image was acquired by positioning the bottom scope objective close to the sample and the top scope objective a distance of $1.5\mu\text{m}$ away from the sample. In panel a (panel c) for the bead highlighted with an arrow, the number of photons detected in the bottom and top scope images are 4750 and 8770 (3600 and 5900), respectively. In panel b for the QD label highlighted with an arrow, the number of detected photons in the bottom scope and top scope images are 3100 and 8700, respectively. In all panels the rightmost column shows cropped images of the nanoprobe that are highlighted with an arrow in the left and center columns. The images shown are the raw data that are not spatially registered. Because of the use of different detectors to capture the images in the top and bottom scopes, there is a scale change between the bottom scope and top scope images. In all the panels, the nanoprobe images are numbered to aid visualization. Scale bar = $5\mu\text{m}$.

the non-uniform nature of drift in both x and y directions and also due to the fact that the drift correction algorithm is influenced by the noisy nature of the data. Similar issues concerning residual stage drift and standard deviation of x-y coordinates have been previously reported in the literature (e.g., see [46]).

Table 1. Results of 2D location estimation from dMUM images. The table lists the standard deviation (std-dev) and the 2D localization measure (loc-meas) for the X/Y coordinate of 100 nm tetraspeck beads that were imaged in the 2D infocus imaging configuration. The X-Y estimates for dMUM were determined using the estimation algorithm described in Section 2.4. The X-Y estimates for the top and bottom scopes were independently determined by fitting Airy profiles to the corresponding images. All X-Y coordinates were drift corrected prior to calculating the standard deviation. For each nanoprobe sample, the standard deviation was calculated from 80 estimates. The 2D localization measure for each bead was computed as described in Section 2.6.

Bead #	Std-dev of x_0 , bottom scope [nm]	Std-dev of y_0 , bottom scope [nm]	Loc-meas of x_0/y_0 , bottom scope [nm]	Std-dev of x_0 , top scope [nm]	Std-dev of y_0 , top scope [nm]	Loc-meas of x_0/y_0 , top scope [nm]	Std-dev of x_0 , dMUM scope [nm]	Std-dev of y_0 , dMUM scope [nm]	Loc-meas of x_0/y_0 , dMUM scope [nm]
1	4.8	4.3	4.5	5.4	5.4	5.7	3.8	3.3	3.5
2	4.4	3.8	4.2	5.8	5.4	5.7	3.5	3.4	3.4
3	4.0	3.5	3.4	4.5	5.5	4.2	3.0	2.7	2.6
4	4.3	3.9	4.1	5.5	5.4	5.1	3.3	3.1	3.2

3.3.1. 2D localization measure of dMUM and standard microscope - analytical calculations for the 2D infocus imaging configuration

In the previous section, we showed that for the 2D infocus imaging configuration, our proposed algorithm can determine the X-Y coordinates from dMUM with consistently better accuracy when compared to estimates obtained from a standard microscope. A common question that arises when designing an estimation algorithm is what is the best possible accuracy with which the unknown parameters of interest can be determined and whether a particular algorithm can attain this accuracy. Here, we have carried out a statistical analysis based on the Fisher information matrix, which provides a quantitative measure of the total information contained in the acquired data about the parameters that we wish to estimate (see Section 2.6). Specifically, we calculate the 2D localization measure of an infocus point source for dMUM and for a standard microscope.

Table 1 lists the 2D localization measures of the different microscope setups for each nanoprobe. For all the microscope setups, we see that the predicted accuracy (2D localization measure) is consistently close to the experimental accuracy (standard deviation of the X-Y estimates). In some cases, we see that the predicted accuracy is larger (smaller) than the experimental accuracy. This is in part due to the finite number of samples used to calculate the standard deviations. It should be pointed out that the predicted accuracy is an analytically calculated result of the expected value of the standard deviation, whereas the experimental accuracy is a finite sample estimate of the standard deviation. Results from large sample statistics guarantee that with sufficiently large number of estimates the experimental accuracy converges to the theoretical accuracy ([45]). In the present manuscript, due to several practical considerations (photobleaching, focus drift, etc) the number of images that was used to calculate the experimental accuracy was limited to 80. This accounts for the observed variability of the ex-

perimental accuracy with respect to the predicted accuracy. Note that the predicted accuracy for the bottom scope is consistently smaller than the predicted accuracy for the top scope. This is in agreement with the behavior of the standard deviations of the X-Y estimates for the two microscope configurations, which we noted in Section 3.3.

Fig. 3(a) shows the variation of the 2D localization measure for an infocus point source as a function of the expected number of detected photons for dMUM and for a standard microscope in the 2D infocus imaging configuration. From the figure we see that for a range of photon counts, the numerical value of the 2D localization measure for dMUM is consistently smaller than that of the standard microscope. An immediate implication of this result is that the 2D location of an infocus nanoprobe can be determined with better accuracy in dMUM than in a standard microscope. For example, for the practical experimental conditions considered in Fig. 3(a), in a standard microscope the 2D location of the nanoprobe can be determined with an accuracy no better than ± 12 nm when 2000 photons are collected from the nanoprobe per image. On the other hand, in dMUM if 2000 photons are collected from the nanoprobe per image in the top and bottom scopes, then the 2D location of that nanoprobe can be determined with an accuracy no better than ± 8.5 nm.

3.4. *Estimating z-location from dMUM - 3D imaging configuration, and comparison to standard microscope and MUM*

We next investigated the z-localization capability of dMUM. For this, we imaged bead samples in dMUM using the 3D imaging configuration (see Fig 2(c)). For z-estimation, we made use of the z-localization algorithm MUMLA, which we developed for z-position determination from multifocal plane images (see Section 2.5). We applied MUMLA to the bead images highlighted with an arrow in Fig. 2(c). The mean and standard deviation of the z-position estimates for this bead were 247 nm and 8 nm, respectively.

We next compared the z-localization capabilities of dMUM, MUM and a standard microscope. For each microscope configuration, we calculate the 3D localization measure of z_0 , which provides a limit to the accuracy with which the z-position can be determined. Fig. 3(b) shows the results of our calculation as a function of z-position. In [9, 38] we had reported the 3D localization measure calculations for MUM and a standard microscope. Consistent with these results, we see that a standard microscope exhibits poor z-localization accuracy, especially near the plane of focus. On the other hand, both MUM and dMUM exhibit consistently better z-localization accuracy than a standard microscope for a range of z-values including near the plane of focus. Both MUM and dMUM capture images of a point source at different focus levels (see Fig. 4), which provide significant additional information that constrains the z-estimation leading to the improved accuracy.

Note that the z-localization capability of dMUM is uniformly better than that of MUM. This is because in MUM the fluorescence signal from the sample is collected from only one objective (see Fig. 4). Hence dMUM collects more photons from the sample than MUM resulting in better z-accuracy. To validate this, we carried out z-estimation on simulated dMUM and MUM images using MUMLA. Fig. 5 shows the plot of the z-estimates for different z-positions and Table 2 lists the standard deviations of the estimates. From the table it can be seen that consistent with the 3D localization measure calculations, the accuracy of the z-estimates for dMUM is uniformly better than that of MUM.

3.5. *Effect of focal plane spacing on the 3D localization measure*

In the previous section, we showed that dMUM provides consistently better accuracy than MUM and a standard microscope in determining the z-location of a point source for a range of z_0 values. We next investigated how the focal plane spacing affects the 3D localization mea-

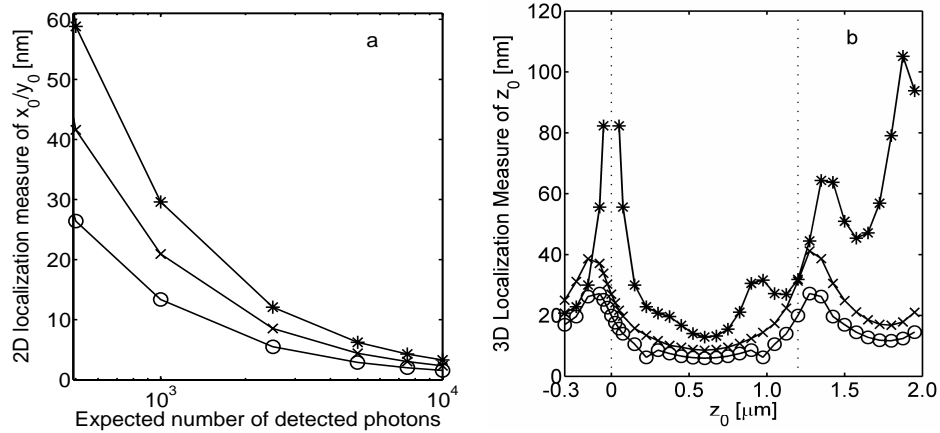


Fig. 3. Localization measure calculations for different microscope configurations. Panel a shows the variation of the 2D localization measure of x_0/y_0 coordinate as a function of the expected number of detected photons for dMUM (×,○) and for a standard microscope (*). Here, the photon detection rate for the standard microscope is set to 10,000 photons/s. For dMUM we consider two scenarios, one where we have the same photon detection rate of 10000 photons/s for the top and bottom scopes (×) and the other where we have different photon detection rates of 20000 photons/s and 10000 photon/s for the top and bottom scopes, respectively (○). The latter scenario of unequal photon detection rates occurs in our experimental data (Fig. 2). The following are the numerical values of the other parameters that are used to generate the plots in this panel: $n_a = 1.2$, $M = 63$, $\lambda = 555$ nm, the pixel array size is 11×11 , the pixel size is $12.9 \mu m \times 12.9 \mu m$, the background component is 300 photons/pixel/s, the mean and standard deviation of the readout noise of the imaging detector are $0 e^-/\text{pixel}$ and $8 e^-/\text{pixel}$, respectively, the X-Y coordinate of the nanoprobe is assumed to coincide with the center of the pixel array, and the noise statistics is assumed to be the same for all pixels. The x-axis range denotes the expected number of detected photons in the bottom scope which corresponds to an acquisition time range of 0.01 s to 1 s.

Panel b shows the variation of the 3D localization measure of z_0 as a function of the z -position for dMUM (○), for two plane MUM (×) and for a standard microscope (*). The vertical dotted lines indicate the position of the two focal planes ($0 \mu m$ and $1.2 \mu m$) that are simultaneously imaged in dMUM/MUM. The photon detection rate and background component for the standard microscope are set to 10000 photons/s and 600 photons/pixel/s, respectively. In MUM, the photons collected by the objective are split by a 50:50 beam splitter. Hence for the two plane MUM setup, the photon detection rate and background component are set to 5000 photon/s per plane and 300 photons/pixel/s per plane, respectively. In dMUM, the photon detection rate and the background component are set to 10000 photons/s and 600 photons/pixel/s, respectively for both the top and bottom scopes. For all the microscope configurations, the exposure time is set to 0.5 s and all other numerical values are identical to those used in panel a.

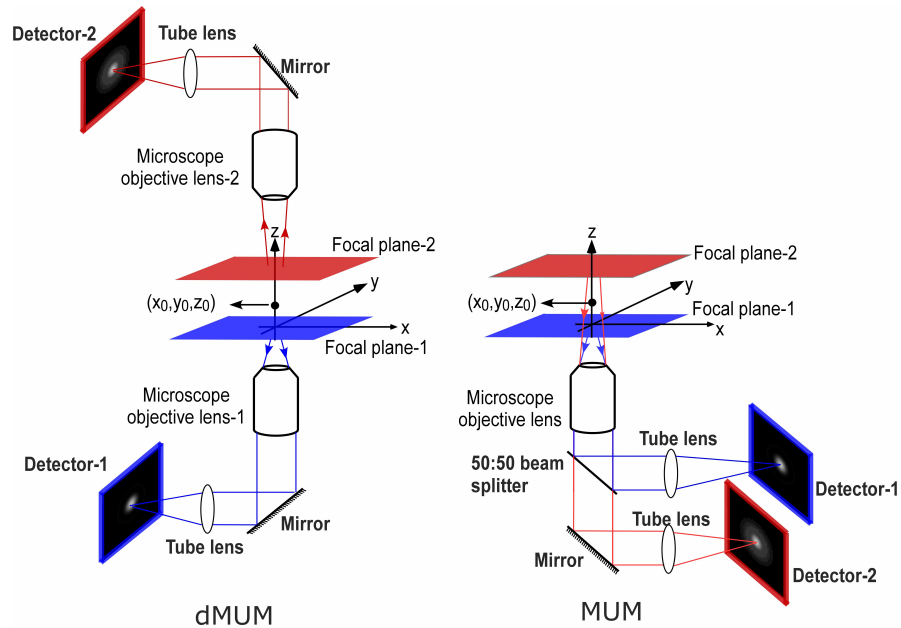


Fig. 4. Schematic showing the 3D imaging configuration of dMUM and MUM. Both dMUM and MUM support simultaneous imaging of different focal planes. In dMUM the fluorescence signal is collected from above and below the sample by two different objective lenses, each of which is positioned such that they image a distinct focal plane. In MUM the fluorescence signal is detected from only one side of the sample. The collected signal is then split into two detectors, where each detector is placed at a specific calibrated distance from the tube lens.

sure of z_0 for dMUM. Fig. 6 shows the results of the 3D localization measure calculations for different focal plane spacings for dMUM. Here, the number of photons detected in the top and bottom scopes are assumed to be the same for all the focal plane spacings and we consider three different focal plane spacings of $1\mu\text{m}$, $1.25\mu\text{m}$ and $1.5\mu\text{m}$. From the figure we see that among the three focal plane spacings considered, the $1\mu\text{m}$ focal plane spacing has the best 3D localization measure of z_0 for z values in the range of 0 to $0.6\mu\text{m}$, the $1.25\mu\text{m}$ focal plane spacing has the best 3D localization measure of z_0 for z values in the range of $0.6\mu\text{m}$ to $0.8\mu\text{m}$ and the $1.5\mu\text{m}$ focal plane spacing has the best 3D localization measure of z_0 for z values in the range of $0.8\mu\text{m}$ to $1.05\mu\text{m}$. Note that there is no single focal plane spacing for which the 3D localization measure of z_0 is consistently the best over the 0 - $1.05\mu\text{m}$ range. An immediate implication of this result is that the accuracy with which the z -location of a point source can be determined is not only dependent on the number of detected photons, but also on other factors such as the focal plane spacing, which is an important aspect that needs to be considered when using dMUM for 3D single particle tracking applications. It should be pointed out that the optimal plane spacing is dependent on the specifics of the experimental setup and may vary for different experimental configurations. This includes the use of an appropriate 3D PSF model. For example, in the presence of refractive index mismatches in the sample the Gibson-Lanni model ([47]) or the vectorial PSF model by Török ([48]) might be more appropriate.

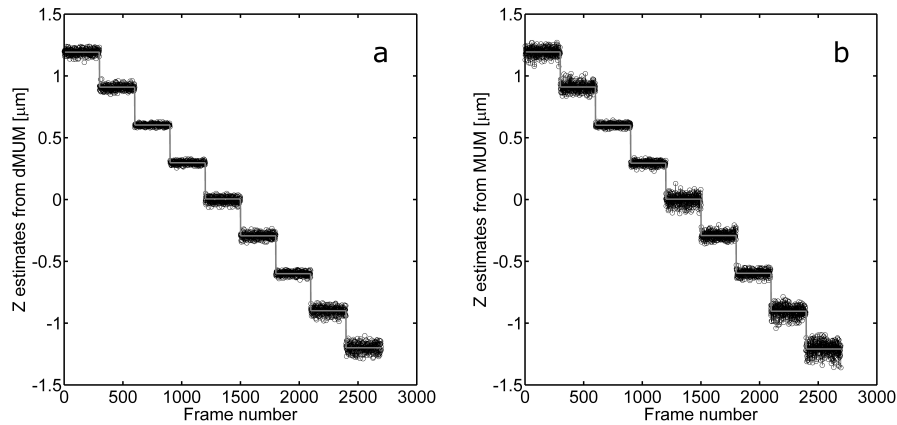


Fig. 5. Results of z-position estimation. The figure shows the z-position (z_0) estimates from simulated images whose means and standard deviations are listed in Table 2. Panel a shows the z-position estimates from dMUM images and panel b shows the z-position estimates from MUM images. In both panels, (—) indicates the mean value of the z-position estimates.

4. Discussion

Single particle imaging approaches have become powerful tools for studying cellular processes due to several advantages they offer over conventional bulk imaging techniques. One of the important factors in conducting single particle imaging experiments is that a sufficient number of photons be detected from the fluorescent label. This is important not only for visually identifying and tracking the labeled entity, but also has implications in the quantitative analysis of the data. We have introduced a new microscope imaging configuration dMUM for single particle imaging in 2D and 3D. The dMUM configuration uses two objective lenses and collects photons from above and below the sample. That the dMUM has improved light collection capability is evident from its optical configuration and, here, we have verified this experimentally. However, an important question arises as to how one can exploit the additional photon counts available in the dMUM images to obtain improved performance. Equally important is the question of how to quantitatively assess the level of improvement that can be attained from the dMUM images. That latter is especially relevant, for example, for designing experimental setups and for evaluating the feasibility of carrying out a particular experiment. In this manuscript, we have addressed these issues by using newly developed tools as well as previously established methodologies and have demonstrated the improved performance of dMUM through experimental data, simulations and analytical calculations.

We have considered two imaging configurations of dMUM, namely the 2D infocus imaging and the 3D imaging configurations. The 2D infocus imaging configuration can be used in place of the classical 2D conventional microscope to image processes that are typically confined to two dimensions. The 3D imaging configuration exploits the multifocal plane imaging capability of dMUM in which the sample is simultaneously imaged at two different focus levels and can be used for 3D tracking applications.

We have developed a new algorithm to determine the X-Y coordinates of nanoprobe from images acquired in the 2D infocus imaging configuration. Using experimental data we have showed that the X-Y coordinates of nanoprobe from their infocus images can be determined with better accuracy with dMUM than with a standard microscope. We have presented ana-

Table 2. Results of 3D location estimation from dMUM and MUM images. The table lists the z-position (z_0), standard deviation (std-dev) of z-position estimates and the 3D localization measure (loc-meas) of z_0 for dMUM/MUM. For each value of z_0 , 300 dMUM/MUM images were simulated and the z-position was estimated from these images using MUMLA (see section 2.5). Fig. 5 shows the plot of the z-position estimates for each z_0 value for dMUM and MUM. The following numerical values were used to simulate the dMUM images. The wavelength of the detected photons was set to 525 nm, the numerical aperture and magnification of the bottom (top) scope objective were set to 1.2 and 63x (62.7x), respectively, the photon detection rate and background component for the bottom (top) scope were set to 3000 photon/s and 400 photons/pixel/s, respectively, the exposure time was set to 1 s, the pixel array size was set to 11×11 , the pixel size was set to $12.9 \mu\text{m} \times 12.9 \mu\text{m}$, the nanoprobe image was assumed to be at the center of the pixel array, the mean and standard deviation of the readout noise in the bottom (top) scope image were set to $0 e^-/\text{pixel}$ and $8 e^-/\text{pixel}$ ($6 e^-/\text{pixel}$), respectively, and the plane spacing between the two focal planes was set to 1000 nm. The numerical values used to simulate the MUM images were identical to those used for simulating dMUM images, except that the photon detection rate and background component for the two focal planes were set to 1500 photon/s and 200 photons/pixel/s, respectively.

Defocus level	True value of z_0 [nm]	Std-dev of z_0 DMUM [nm]	3D loc-meas of z_0 DMUM [nm]	Std-dev of z_0 MUM [nm]	3D loc-meas of z_0 MUM [nm]
1	-1200	36	36	51	54
2	-900	30	29	42	43
3	-600	16	15	23	22
4	-300	21	19	28	28
5	0	23	29	40	40
6	300	13	11	17	17
7	600	10	10	14	14
8	900	21	22	33	33
9	1200	23	23	33	33

lytical calculations to compute the 2D localization measure, which provides a limit to the 2D localization accuracy of an infocus nanoprobe for a given microscope setup. Our calculations show that the new algorithm attains this limit thereby validating that this algorithm indeed provides the best possible accuracy.

While the 2D infocus imaging configuration provides improved x-y localization accuracy, it is not well suited for z-localization. This is due to the poor depth discrimination property that is intrinsic to this imaging configuration. Hence we considered the 3D imaging configuration of dMUM for z-location estimation. We have reported analytical calculations to compute the 3D localization measure of z_0 , which provides a limit to the z-localization accuracy of a nanoprobe for a given microscope setup. Using this, we have compared the z-localization capabilities of three different microscope setups, i.e., dMUM, MUM and a standard microscope. Our results showed that for the 3D imaging configuration dMUM provides uniformly better z-localization accuracy when compared to a standard microscope and MUM. Further, we validated the improved z-localization capability of dMUM over MUM through simulated data, where we showed that the accuracy of the z-estimates from dMUM is consistently better than the accuracy of the z-estimates from MUM.

In [9] we showed that the z-localization algorithm MUMLA is optimal for MUM data in the

sense of attaining the lowest possible standard deviation as specified by the corresponding 3D localization measure. Here, we have shown that with minor modifications the same algorithm can also be applied to dMUM data from the 3D imaging configuration for z-position estimation. A comparison of standard deviations of z-estimates from a simulation study with the 3D localization measures for this dMUM configuration confirmed that MUMLA is also optimal for this setting. Although not discussed here in detail, in the 3D imaging configuration x-y location estimation can be carried out by fitting an appropriate profile to suitably registered images of either the top scope or the bottom scope, analogous to the approach proposed for MUM data analysis in [9]. With this approach we can expect the x-y localization performance to be similar to what can be achieved with a standard microscope. Alternatively, x-y location estimation could be carried out by suitably modifying the x-y localization algorithm for the 2D infocus imaging configuration, by fitting 3D PSF models rather than infocus Airy profiles. In this case we can expect improved x-y localization performance over imaging with a standard microscope in situations when the image of the point source can be detected in the images of both focal planes.

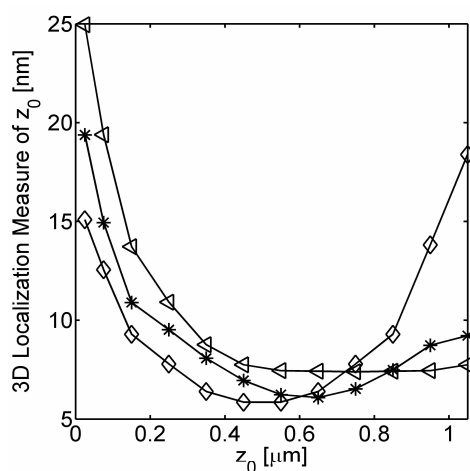


Fig. 6. Effect of focal plane spacing on the 3D localization measure of dMUM. The figure shows the variation of the 3D localization measure of z_0 for dMUM as a function of the z-position for different plane spacing values of $1.0 \mu\text{m}$ (◇), $1.25 \mu\text{m}$ (*) and $1.5 \mu\text{m}$ (◁). All numerical values used to generate the above plots are identical to those used in Fig. 3(b).

In the 2D infocus imaging configuration, we have used the Airy profile ([44]) to describe the image of the nanoprobe. In some situations, the use of an Airy profile may not be suitable, for example, in the case of polarized illumination and/or detection. In such cases, the Airy profile needs to be replaced by the appropriate image profile. In the same way, for the 3D imaging configuration we have made use of the diffraction limited 3D PSF profile that is based on the Born and Wolf model. Depending upon the specific imaging conditions, other 3D PSF image profiles may need to be used. Similar considerations also apply to other aspects of our data analysis, for example, in the use of a background estimation algorithm. It can be deduced from the analytical formula given in Eq. 3 that indeed the improved localization accuracy of dMUM will hold even if other image profiles and/or background estimation procedures need to be used.

The dMUM setup was built using commercially available, off-the-shelf components and is straightforward to implement with little or no customization. The dMUM configuration reported here supports simultaneous imaging of two focal planes. In general, more than two focal planes can be simultaneously imaged with dMUM. This can be achieved by implementing the

MUM imaging configuration in the top and bottom scopes of dMUM. In our implementation of dMUM, we have placed one of the microscopes on top of the other in an upside down orientation. However, other configurations are also possible and our algorithms and analytical calculations can be used with little or no modifications. For example, an alternative configuration for dMUM is to place two inverted microscopes next to each other. The sample is placed in one of the microscopes (bottom scope) and the objective lens in that microscope illuminates the sample and collects the light from the bottom side of the sample. In the other microscope (top scope), the objective lens is attached to the nose piece through an extension arm which positions the objective lens on top of the sample.

The dMUM imaging configuration is not limited to single particle imaging applications. For example, it can be used to improve the photon collection efficiency in a wide variety of low-light level cellular imaging applications including but not limited to the tracking of single molecules, vesicles and viruses in a live cell environment. For the fitting of larger objects, the use of point-source image profiles (Airy profile and 3D point spread function profile) may not be appropriate but can be replaced by a profile that describes the image of the object being tracked. In conclusion, the dMUM imaging configuration permits high accuracy localization of individual nanoprobe in 2D and 3D.

Acknowledgments

This work was supported in part by the National Institutes of Health (R01 GM071048, R01 GM085575 and R01 AI039167) and in part by a postdoctoral fellowship from the National Multiple Sclerosis Society (FG 1798-A-1).